



## Research paper

## Modeling of corner-filletted flexure hinges under various loads

Felix Harfensteller<sup>a,\*</sup>, Stefan Henning<sup>b</sup>, Lena Zentner<sup>b</sup>, Stephan Husung<sup>a</sup><sup>a</sup> Product and Systems Engineering Group, Department of Mechanical Engineering, Technische Universität Ilmenau, P.O. Box 100565, 98684 Ilmenau, Germany<sup>b</sup> Compliant Systems Group, Department of Mechanical Engineering, Technische Universität Ilmenau, P.O. Box 100565, 98684 Ilmenau, Germany

## ARTICLE INFO

## MSC:

74-10  
74S05  
74S99  
74K10

## Keywords:

Compliant mechanism  
Flexure hinge  
Finite element method  
Analytical model

## ABSTRACT

Compliant mechanisms are widely applied in precision engineering, measurement technology and microtechnology, due to their potential for the reduction of mass and assembly effort through the integration of functions into fewer parts and an increasing motion repeatability through less backlash and wear, if designed appropriately. However, a challenge during the design process is the handling of the multitude of geometric parameters and the complex relations between loads, deformations and strains. Furthermore, some tasks such as the dimensioning by means of optimization or the modeling for a controller design require a high number of analysis calculations. From this arises the need for sufficient computational analysis models with low calculation time. Existing studies of analysis models are mostly based on selected load cases, which may limit their general validity. The scope of this article is the comparison of models for the analysis of corner-filletted flexure hinges under various loads, to determine their advantages, disadvantages and application fields. The underlying methods of the study can further be used to evaluate future models based on a broad selection of possible load cases.

## 1. Introduction

Compliant mechanisms achieve motion through the flexibility of their elements [1]. In the case of monolithic compliant mechanisms, these elements are manufactured as one single piece of material. This integration of functions into fewer parts enables miniaturization as well as a reduction of mass and assembly effort. By utilization of compliant hinges instead of conventional hinges, surface friction effects can be avoided, which results in increasing motion repeatability through less wear and backlash and no need for lubrication. Due to these advantages, compliant mechanisms have great potential in precision engineering, microtechnology, bionics, measurement and medical technology. Established applications include for example positioning stages and amplification mechanisms for piezo actuators [2–4] as well as grippers [5,6]. These mechanisms often contain compliant elements in the form of flexure hinges (see Figs. 1 and 2(a)).

However, the advantages of compliant mechanisms are accompanied by challenges in their design. The mechanical behavior, determined by a multitude of parameters, requires the balancing of often contradictory design goals. Possible geometrical parameters include the mechanism structure, the hinge positions as well as the hinge shapes (see Fig. 2(a)). In addition, materials and manufacturing processes must be selected accordingly. These parameters and their dependencies influence for example the installation space, motion range, mechanical advantage, load capacity and dynamic behavior. To predict the mechanical properties,

\* Corresponding author.

E-mail addresses: [felix.harfensteller@tu-ilmenau.de](mailto:felix.harfensteller@tu-ilmenau.de) (F. Harfensteller), [stefan.henning@tu-ilmenau.de](mailto:stefan.henning@tu-ilmenau.de) (S. Henning), [lena.zentner@tu-ilmenau.de](mailto:lena.zentner@tu-ilmenau.de) (L. Zentner), [stephan.husung@tu-ilmenau.de](mailto:stephan.husung@tu-ilmenau.de) (S. Husung).URL: <https://www.tu-ilmenau.de/produkt-und-systementwicklung> (F. Harfensteller).<https://doi.org/10.1016/j.mechmachtheory.2022.104937>

Received 10 December 2021; Received in revised form 21 April 2022; Accepted 11 May 2022

Available online 26 May 2022

0094-114X/© 2022 The Author(s). Published by Elsevier Ltd. This is an open access article under the CC BY license (<http://creativecommons.org/licenses/by/4.0/>).

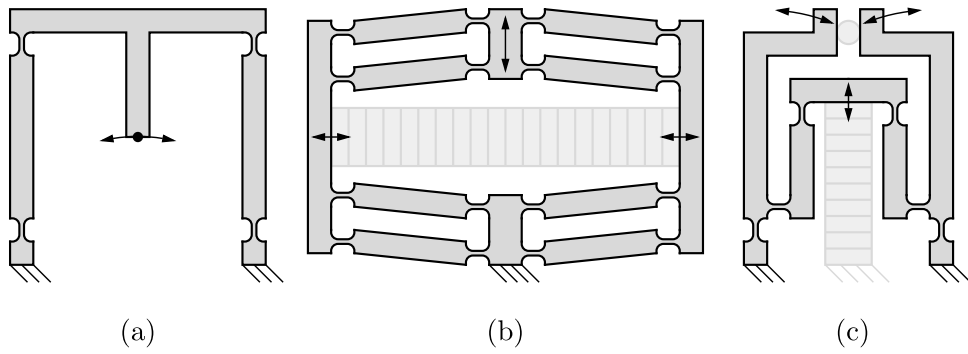


Fig. 1. (a) Parallel-guiding mechanism according to [7], (b) displacement amplifier according to [4] and (c) gripper according to [7] as examples of compliant mechanisms with flexure hinges.

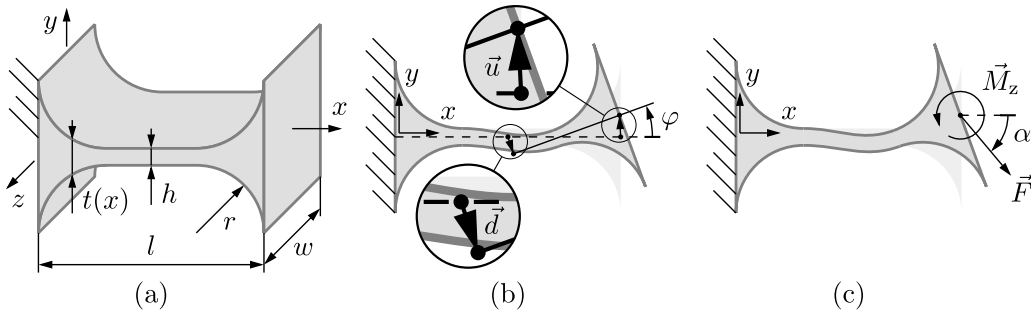


Fig. 2. (a) Dimensions, (b) deflections and (c) loads of investigated models for corner-filletted flexure hinges.

a wide range of analysis approaches can be used and thus support the design process. Among them are for example finite element models [8,9], pseudo-rigid-body models [10,11], beam constraint models [12,13], the compliance matrix method [14,15], continuum beam models [7,16] and design equations [17,18]. Overviews of modeling approaches with regard to various aspects can be found in [19–21]. The calculation time of these models can be decisive for their applicability, especially for a high number of analysis calculations, such as in the dimensioning by means of optimization or the modeling for a controller design. These tasks require analysis models with low calculation time and sufficient accuracy in the prediction of strains, deformations and reaction forces. Comparisons of available models are mostly based on selected load cases and geometric parameters. This may limit their general validity, since the expected accuracy in other possible load cases remains unclear.

This article extends the comparability of various selected models focusing on the analysis of different corner-filletted flexure hinges. The analysis of individual hinges is of great interest due to their significance for the mechanical properties of the overall mechanism and the applicability of the results across different mechanisms. The investigations include the prediction of strains and rotational axis shift under a broad range of rotation angles as well as longitudinal and transversal loads. For this purpose, the selected models are presented first. By means of the design of experiment, different contour shapes and load cases are determined for the following comparison. The results yield conclusions about the advantages, disadvantages and applications of the individual models. The underlying methods of the study can be used to evaluate models based on a broad selection of possible load cases and thereby extend the general validity of future studies.

## 2. Model parameters

Starting point for the investigations are shape variations of corner-filletted flexure hinges, characterized by their length  $l$ , width  $w$ , fillet radius  $r$  and minimum notch height  $h$  (see Fig. 2(a)). The hinge height respectively thickness along the  $x$ -axis is described by  $t(x)$ . The applied material properties correspond to the aluminum alloy ENAW7075 (Young's modulus:  $E = 72000$  MPa, Poisson's ratio:  $\nu = 0.33$ , proof stress:  $R_{p0.2} = 470$  MPa [22]), which is often used in compliant mechanism design [2–6]. One end of the hinge is fixed to the reference frame. Deflections or loads are applied at the opposite end (see Fig. 2(b) and (c)). The displacement vector  $\vec{u}$  is composed of the components  $u_x$  and  $u_y$ . Similarly, the force vector in the direction of the angle  $\alpha$  is composed of the components  $F_x$  and  $F_y$ . Furthermore, the rotation angle of the hinge  $\varphi$  and the torque  $M_z$  are considered. These quantities allow the characterization of a wide variety of loads and displacements at the force application point.

In contrast to idealized revolute hinges, the rotational axis of flexure hinges is not fixed relative to the adjacent links. There are several approaches to model the shift of the rotational axis [23]. In this contribution, the shift is defined as the displacement of the

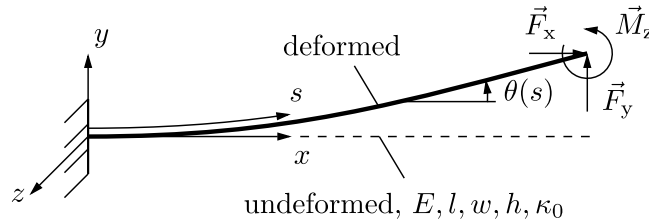


Fig. 3. Deflection of a beam with its geometric and material parameters loaded by two forces  $\vec{F}_x$  and  $\vec{F}_y$  and a torque  $\vec{M}_z$ .

virtual center point (vector norm of  $\vec{d}$  with components  $d_x$  and  $d_y$ ) fixed to the force application point at the deflected end ( $u_x, u_y$ ) of the flexure hinge (see Fig. 2(b)). It is calculated by:

$$d = \sqrt{d_x^2 + d_y^2} \quad \text{with} \quad (1)$$

$$d_x = u_x + \frac{l}{2} \cdot (1 - \cos \varphi) \quad \text{and} \quad d_y = u_y - \frac{l}{2} \cdot \sin \varphi. \quad (2)$$

### 3. Selected modeling approaches

**Overview and abbreviations.** The investigations contained in this article include modeling approaches by:

- compliance matrices based on linear Euler–Bernoulli beam theory (CMat),
- nonlinear continuum Euler–Bernoulli beam models (ConBeam),
- finite Euler–Bernoulli beam element models (FEM 1D),
- finite quadrilateral element models with plane stress (FEM 2D  $\sigma$ ) and plane strain (FEM 2D  $\varepsilon$ ) and
- finite hexahedral element models (FEM 3D).

Please note, that the abbreviations regarding the finite element models (FEM 1D, FEM 2D, FEM 3D) are distinguished by the spatial location of the node positions and not by the degree of freedom of the node deformations. The models are additionally distinguished by geometrically linear (lin.) and nonlinear (n.lin.) behavior.

**Compliance matrices (CMat).** According to Lobontiu [14], the compliance of flexure hinges in different spatial directions can be summarized in matrix notation, where the entities of the matrix are based on the Euler–Bernoulli or Timoshenko beam theory. Each matrix entry ( $C_{11}$ ,  $C_{12}$ ,  $C_{22}$ ,  $C_{33}$ ) describes the compliance regarding a deformation ( $\varphi$ ,  $u_y$ ,  $u_x$ ) with respect to a given load ( $M_z$ ,  $F_y$ ,  $F_x$ ). In the case of plane deformations the matrix results in:

$$\begin{Bmatrix} \varphi \\ u_y \\ u_x \end{Bmatrix} = \begin{bmatrix} C_{11} & C_{12} & 0 \\ C_{12} & C_{22} & 0 \\ 0 & 0 & C_{33} \end{bmatrix} \begin{Bmatrix} M_z \\ F_y \\ F_x \end{Bmatrix} \quad (3)$$

A generalized formulation of this approach for various individual hinges and also mechanisms can be found in [14]. The corresponding implementation in this paper is based on [15], which contains closed-form equations of the matrix entries for corner-filletted flexure hinges. The strain is calculated without further concentration factors at 20 points along the  $x$ -axis by:

$$\varepsilon(x) = \left| \frac{6 \cdot (M_z + F_y \cdot (l - x))}{E \cdot w \cdot t(x)^2} \right| + \left| \frac{F_x}{E \cdot w \cdot t(x)} \right| \quad (4)$$

For the model evaluation, only the maximum strain in the hinge is considered.

**Nonlinear continuum Euler–Bernoulli beam models (ConBeam).** The theory for large deflections of (curved) rod-like structures [1] has extensively been utilized to describe the deformation behavior of flexure hinges and compliant mechanisms under large deflections and was shown to be in good correlation with three-dimensional FEM-based results for certain load cases [7,16]. The model is based on the deformation of a beam loaded by two directionally constant forces  $\vec{F}_x$  and  $\vec{F}_y$  and an external torque  $\vec{M}_z$  as shown in Fig. 3.

The beams dimensions are given by the height  $t(s)$ , the width  $w$  and the length  $l$ . Further, it may be curved in the unloaded state by a curvature  $\kappa_0$ . The material is specified by the Young's modulus  $E$ . Due to the deflection, a bending torque  $M_b$ , an angle  $\theta$ , a curvature  $\kappa$  and displacements in  $x$ - and  $y$ -direction result along the beam axis  $s$ . Considering large deflections, the following system of differential equations results:

$$\frac{dM_b}{ds} = F_x \sin \theta - F_y \cos \theta, \quad (5)$$

$$\frac{d\theta}{ds} = \kappa, \quad \text{with} \quad \kappa = \frac{M_b}{EI_z} + \kappa_0, \quad (6)$$

$$\frac{dx}{ds} = \cos \theta, \quad (7)$$

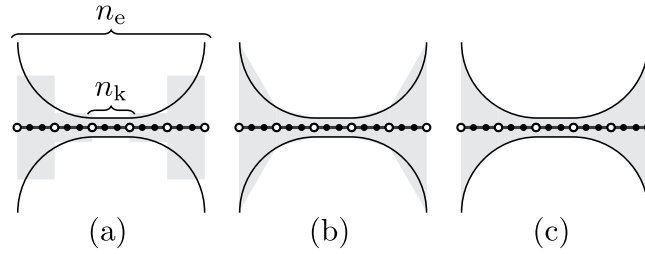


Fig. 4. Approximated hinge contour with (a) constant, (b) tapered or (c) circular cross-sectional profile in fillet section and four nodes per element ( $n_k = 4$ ) and five elements per hinge ( $n_e = 5$ ).

$$\frac{dy}{ds} = \sin \theta. \quad (8)$$

It is worth noticing, that the Young's modulus, the second moment of area  $I_z$  or the curvature in the initial state  $\kappa_0$  do not have to be constant and may be functions of  $s$  for example for the realization of flexure hinge contours. For a single beam with a free end as shown in Fig. 3, the four boundary conditions result:

$$M_b(s = L) = M_z, \quad \theta(s = 0) = 0, \quad x(s = 0) = 0, \quad y(s = 0) = 0. \quad (9)$$

In summary, a boundary value problem results that can be solved numerically using a four-step Runge–Kutta-method in combination with the shooting method [16]. After a solution is obtained, results for each equation are present for each  $s$ . These results can be used to determine the elastic strain, rotational axis shift or displacements.

**Finite Euler–Bernoulli beam element models (FEM1D).** Both linear [24,25] and nonlinear [8,26,27] finite beam elements have been utilized for the analysis of compliant mechanisms. These can be derived from the differential equations of the Euler–Bernoulli beam with the help of the principle of virtual displacement [28]. The finite beam elements in this paper are created based on the description given in [28] (similar to [8,26]). The derivation of these finite beam elements and their combination to a hinge model, require the consideration of several modeling parameters. Among them are the number of nodes per element  $n_k$  and the number of elements per hinge  $n_e$ . For planar beam models, each node provides three degrees of freedom. The axial displacement over the element is interpolated using Lagrange polynomials and the transversal deflection as well as the node rotation are interpolated with Hermite polynomials. The derivation of the stiffness matrices allows the consideration of a variable cross-section along the element. Thus, the contour of the fillet hinge section can be approximated with different cross-sectional profiles, for example with a constant, tapered or circular changing hinge height (see Fig. 4).

The element height of the constant profile ((a) in Fig. 4) corresponds to the arithmetic mean of the hinge heights at both ends of the finite beam element. The tapered profile ((b) in Fig. 4) matches the heights at the ends of the element. The circular changing profile represents the idealized contour of the fillet hinge section exactly ((c) in Fig. 4). The cross-sectional profile, the node number per element and the element number per hinge influence the equations to be solved and their computation time. Therefore, computation time and approximation error must be considered against each other. The Appendix contains a more detailed description of these relations. The results of the finite beam element models in Section 5 are created using elements with tapered and constant cross-sectional profiles with three nodes. At least 14 finite elements per hinge are used. Their nodes are approximately equidistant. Deviations in their distance result from rounding up the element number in the hinge sections (fillet and constant sections), since a node is required at the boundary between the sections respectively between the different finite element types. The system of nonlinear equations to determine the displacements and loads is solved using the Newton method. The Kármán strain (see [28]) is calculated based on the displacements at five equidistant points along the beam axis of each element. The maximum strain in the hinge is considered for the evaluation of the model. All calculations related to the finite Euler–Bernoulli beam element models are implemented in Python®.

**Finite quadrilateral and hexahedral element models (FEM2D and FEM3D).** Two-dimensional and three-dimensional finite element models are common tools for the analysis of compliant mechanisms. But especially for the investigation of a wide range of hinge dimensions, the automatic meshing of the models presents a challenge. High stress gradients in the regions of small notch heights or fillets require a locally high element density. However, these areas are not known in advance and meshing with generally high element density leads to unnecessarily high computational time. In addition, the shape of the elements also has a decisive role in the quality of the results. Depending on the element type, this is evaluated on the basis of various factors, like the element aspect ratio, the size of the corner angles or the Jacobian ratio [29]. A customized meshing strategy enables a suitable element shape and an appropriate computational time for a wide range of hinge dimensions (see Fig. 5).

The element nodes within the  $x$ – $y$ -plane are distributed equidistant along circular arcs that are perpendicular to the contour (see Fig. 5). The length of a circular arc  $e_h$  depends on its position characterized by  $e_c$  (see Fig. 6). The quantity  $e_c$  represents the distance of the arc connection point from the hinge center traced along the contour. In the constant center segment of the hinge, the arc (infinite radius) corresponds to a line and  $e_c$  is identical to the hinge height  $h$ .

The starting point of the meshing strategy is the specification of a number of elements over the height of the hinge  $n_H$ . The intended element length is adaptively calculated by dividing the length of the circular arc  $e_h$  by the number of elements over the

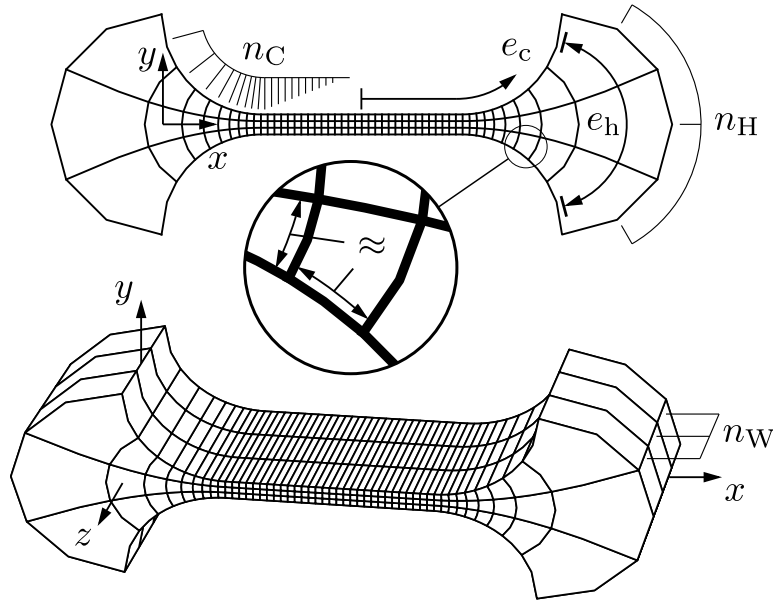


Fig. 5. Meshing parameters for quadrilateral and hexahedral element models.

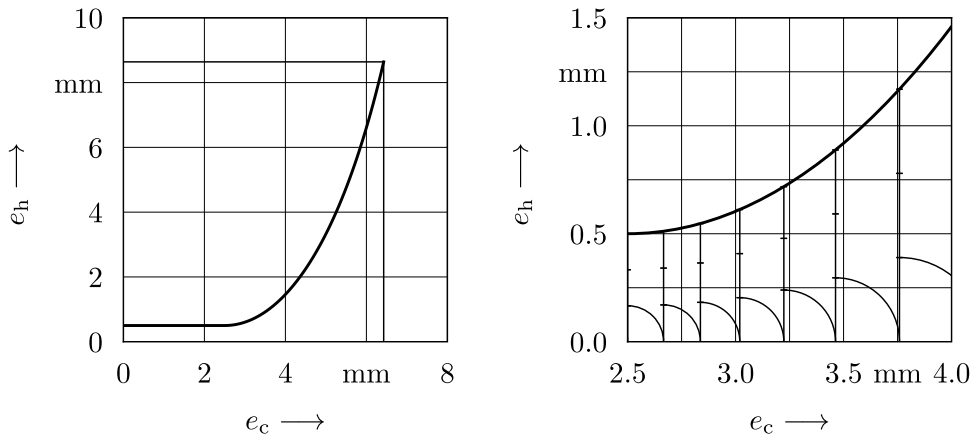


Fig. 6. Length and distance of the circular arcs depending on the position along the contour given by  $e_c$  and the number of elements over the height of the hinge  $n_H = 3$  ( $l = 10$  mm,  $r = 2.5$  mm,  $h = 0.5$  mm).

height  $n_H$ . Starting from the center, each new arc is shifted along the contour by the current intended element length (see Fig. 6). This results in an iterative procedure that distributes the nodes of the elements in approximately equal distances. When the end of the contour is reached, the position of all contour nodes is linearly scaled in direction of  $e_c$ , so that the closest element edge matches the end of the contour.

The number of elements along the height  $n_H$  thus results in the number of elements along the contour  $n_C$ . However, the number of elements along the height is not a suitable parameter to control the meshing, since the element density differs greatly between hinges with small or large notch height. For this reason, the described procedure is repeated with an increasing number of elements over the height until a minimum number of elements in the  $x$ - $y$ -plane  $n_{HC,min}$  is reached ( $n_H \cdot n_C \geq n_{HC,min}$ ).

This strategy allows the evenly meshing of different hinge contours in the  $x$ - $y$ -plane, which suffices for the use of quadrilateral elements. The same strategy is used for the modeling with hexahedral elements, by projection of the mesh in  $z$ -direction, which additionally requires the determination of the element number along the hinge width  $n_W$ . This element number is calculated from the desired edge length in  $z$  direction by means of the geometric mean of the minimal and maximal edge length in the  $x$ - $y$ -plane. This minimizes the extrema of aspect ratios (largest edge length divided by smallest edge length of an element) in the overall mesh. Since the number of elements in  $z$  direction is less crucial for the calculation results, due to the planar load case, a maximum number of elements along the hinge width is defined to reduce the calculation time ( $n_W \leq n_{W,max}$ ).

**Table 1**  
Parameters of design of experiments.

Parameter	Value range
Hinge radius relative to length	$0.05 \leq r_i/l \leq 0.5$
Hinge notch height relative to length	$0.01 \leq h_i/l \leq 0.2$
Intended utilization ratio	$0.1 \leq \eta_i \leq 1.0$
Intended strain ratio due to the rotation angle	$0 \leq \zeta_i \leq 1$
Angle of hinge force	$-\pi \leq \alpha_i \leq \pi$

The finite quadrilateral and hexahedral element models are implemented in *ANSYS Mechanical™ APDL 2021 R1* using *PLANE183* and *SOLID186* elements. The associated *APDL* batch files are created by automated scripts that define node positions, finite elements, boundary conditions and loads. The maximum equivalent von Mises strain of all elements is considered for the evaluation of the model. Based on a meshing study, the meshing parameters are defined as  $n_{HC,min} = 1000$  and  $n_{W,max} = 30$ . According to the boundary conditions, one end of the hinge (circular arc or cylindrical surfaces) is fixed. For the load application in analogy to the beam model, all nodes of the opposite end are rigidly connected to a pilot node in their center (see Fig. 7).

#### 4. Design of experiments

In order to cover a wide range of relevant hinge dimensions and load cases, a staged parameter definition is performed, which takes the relationship between the maximum admissible loads of each individual set of hinge dimensions into account. Quantities specific to a given parameter set are labeled in the following by the additional index  $i$ .

The hinge length is used as a reference for the remaining dimensions to obtain dimensionless ratio parameters. For this purpose, the hinge length is fixed to  $l = 10$  mm. In order to reduce the number of calculations and to guarantee a suitable meshing of the models, the ratio of the hinge width relative to the length of the hinge is set to  $w/l = 1$ . The results of the investigations can nevertheless be transferred to hinges with different length or width. The effects of the restrictions will be discussed in greater detail in Section 6.

The ratios of the radius and notch height relative to the length of the hinge are varied in the range of  $0.05 \leq r_i/l \leq 0.5$  and  $0.01 \leq h_i/l \leq 0.2$  (see Fig. 2(a)). This covers a wide range of typical applications [2–6]. An exception are very thin hinges in load cells, which are only subject to very selected load cases with almost no deflection and are designed with specialized goals. More detailed considerations in this regard can be found in [9].

Since the values of admissible loads ( $\varphi_i$ ,  $F_{x,i}$ ,  $F_{y,i}$ ) strongly depend on the joint geometry defined by  $r_i/l$  and  $h_i/l$ , three additional geometry-independent load parameters are used to define suitable load cases. These include the intended utilization ratio  $\eta_i = \varepsilon_i/\varepsilon_{p0.2}$ , which is calculated as the quotient of the intended maximum strain of the particular parameter set ( $\varepsilon_i$ ) and the strain at the offset yield point ( $\varepsilon_{p0.2} = R_{p0.2}/E$ ). By varying the intended utilization ratio in the range of  $0.1 \leq \eta_i \leq 1.0$ , it is ensured that both low and high strains are investigated.

A further distinction is made according to the cause of the strain. For this purpose,  $0 \leq \zeta_i \leq 1$  is introduced as the ratio of the maximum hinge strain due to the angle of rotation. The ratio of  $\zeta_i = 1$  indicates for a given parameter set, that the strain is exclusively caused by the rotation angle and no other hinge forces are present. Accordingly, the ratio of  $\zeta_i = 0$  indicates, that the strain is exclusively caused by hinge forces.

The third load parameter  $\alpha_i$  defines the direction of the hinge force. It is varied in the range of  $-\pi \leq \alpha_i \leq \pi$ .

The two geometric parameters ( $r_i/l$ ,  $h_i/l$ ) and three load parameters ( $\eta_i$ ,  $\zeta_i$  and  $\alpha_i$ ) span a parameter space, which is summarized in Table 1. Within this parameter space, 100 parameter sets are selected using latin hypercube sampling. The exact parameter values are listed in the accompanying file in [30]. For each of the parameter sets, two load calculations are performed to determine the values of  $\varphi_i$ ,  $F_{x,i}$  and  $F_{y,i}$  using the linear quadrilateral element model (lin.FEM 2D  $\varepsilon$ , see Fig. 7). The use of a linear test model allows the robust and fast estimation of appropriate loads, by avoiding potential non-continuous results (e. g. due to buckling) and non-convergence, which may occur with nonlinear models. Quantities associated with these load calculations are labeled in the following by the additional index  $t$ .

The first load calculation estimates the relation between the rotation angle of the parameter set  $\varphi_i$  and the resulting strain. For this purpose a testing strain  $\varepsilon_{\varphi,t}$  is determined for the given hinge contour of the parameter set ( $r_i/l$ ,  $h_i/l$ ) and the application of a testing rotation angle  $\varphi_t = 30^\circ$  without further hinge forces. The test model approximates a linear relation between the rotation angle and the resulting strain. The rotation angle of the parameter set  $\varphi_i$  can thus be calculated from the intended strain due to the rotation angle ( $\varepsilon_{p0.2} \cdot \eta_i \cdot \zeta_i$ ):

$$\varphi_i = \varepsilon_{p0.2} \cdot \eta_i \cdot \zeta_i \cdot \frac{\varphi_t}{\varepsilon_{\varphi,t}} \quad (10)$$

The second load calculation estimates the increase in strain due to an additional hinge force. Therefore a further testing strain  $\varepsilon_{F,t}$  is determined resulting from the calculated angle of rotation  $\varphi_i$  and an additional testing hinge force  $F_t = 1$  kN in the direction of the angle  $\alpha_i$ . The magnitude of the testing rotation angle  $\varphi_t$  and the testing hinge force  $F_t$  is mainly relevant for the numerical errors of the load calculation, since the real hinge behavior may exhibit geometrically nonlinear effects but a linear model is used for the load calculations. So analogously to the first load calculation, a linear relationship is approximated between the magnitude

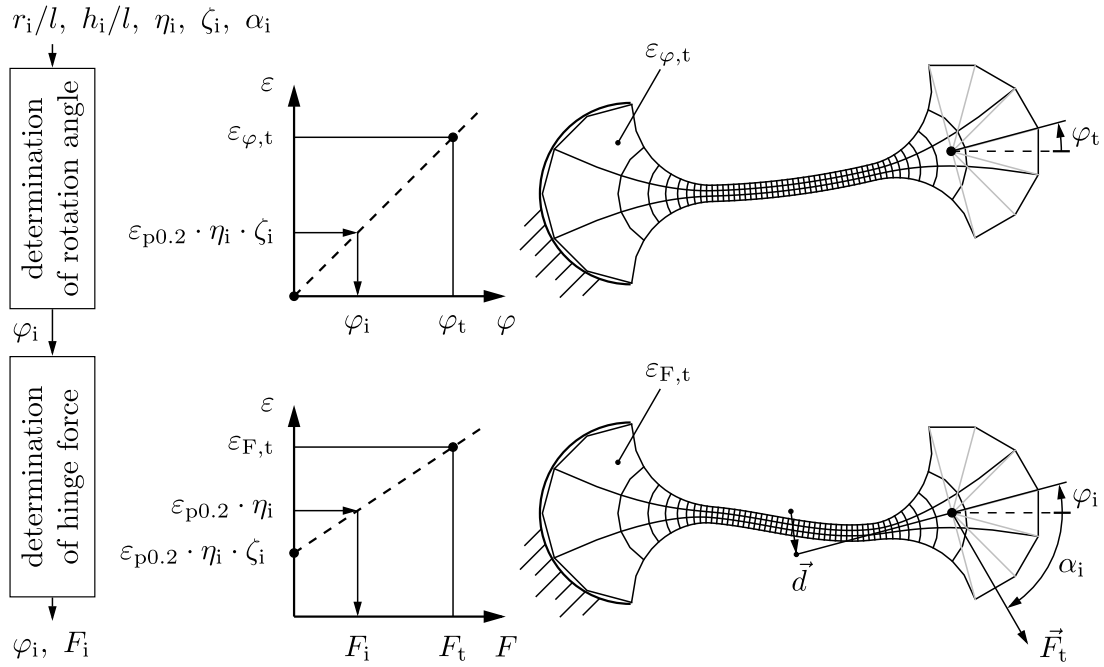


Fig. 7. Determination of the load values by a linear quadrilateral element model.

of the hinge force and the resulting increase in strain. Based on the intended strain due to all loads of the parameter set ( $\varepsilon_{p0.2} \cdot \eta_i$ ), the magnitude of the hinge force  $F_i$  is calculated by:

$$F_i = \varepsilon_{p0.2} \cdot \eta_i \cdot (1 - \zeta_i) \cdot \frac{\varepsilon_{F,t} - \varepsilon_{p0.2} \cdot \eta_i \cdot \zeta_i}{F_t} \quad (11)$$

In this manner, all loads ( $\varphi_i$ ,  $F_i$ ,  $\alpha_i$  respectively  $\varphi_i$ ,  $F_{x,i}$ ,  $F_{y,i}$ ) are determined for each parameter set, which can be applied in the investigated models. The linearization due to the linear test model causes a deviation from the target load case of the parameter set defined by  $\eta_i$  and  $\zeta_i$ . This deviation can be estimated from the results of the study (see lin. FEM 2D  $\varepsilon$  in Fig. 8) and is considered to be sufficiently small.

## 5. Results

Based on the experiment design and the load calculation, the investigated models are applied to the 100 parameter sets. The reference for the comparison of the models is the geometric nonlinear finite hexahedral element model (n. lin. FEM 3D) in ANSYS Mechanical APDL 2021 R1. Quantities associated with this reference model are labeled in the following by the additional index *ref*. Quantities associated with the models evaluated in relation to the reference model are labeled by the additional index *m*. Figs. 8 and 9 show the signed percentage error of the maximum hinge strain and the rotational axis shift for the evaluated models. The different models are listed along the abscissa. The signed percentage error is shown along the ordinate in a boxplot. The box center line indicates the median. The box itself encloses the lower and upper quartile. The whiskers include the values that are within 1.5 times the interquartile range beyond the lower and upper quartiles. Values outside this range are marked with circles as outliers. The signed percentage error (signed relative error in percent) of an evaluated model for the given quantity *q* is calculated by:

$$PE_q = 100 \% \cdot \frac{q_{ref} - q_m}{q_{ref}} \quad (12)$$

In addition, Table 2 lists the median and the interquartile range of the signed percent error of the maximum hinge strain ( $MEPE_\varepsilon$ ,  $IQRPE_\varepsilon$ ) and rotational axis shift ( $MEPE_d$ ,  $IQRPE_d$ ) as well as the mean computational time ratio ( $\overline{t_{ref}/t_m}$ ). The quotient of the mean calculation time of the reference model and the evaluated model, can be interpreted as time gain factor of the evaluated model. The results of each model for all parameter sets are listed in the accompanying file in [30].

## 6. Conclusions

Figs. 8 and 9 illustrate, that the error of the maximum hinge strain and rotational axis shift strongly depend on the particular model and the load case. This confirms the necessity to compare models for the analysis of compliant hinges based on a wide selection of load cases. The dispersion of the error decreases with increasing degrees of freedom of the model, since the investigated

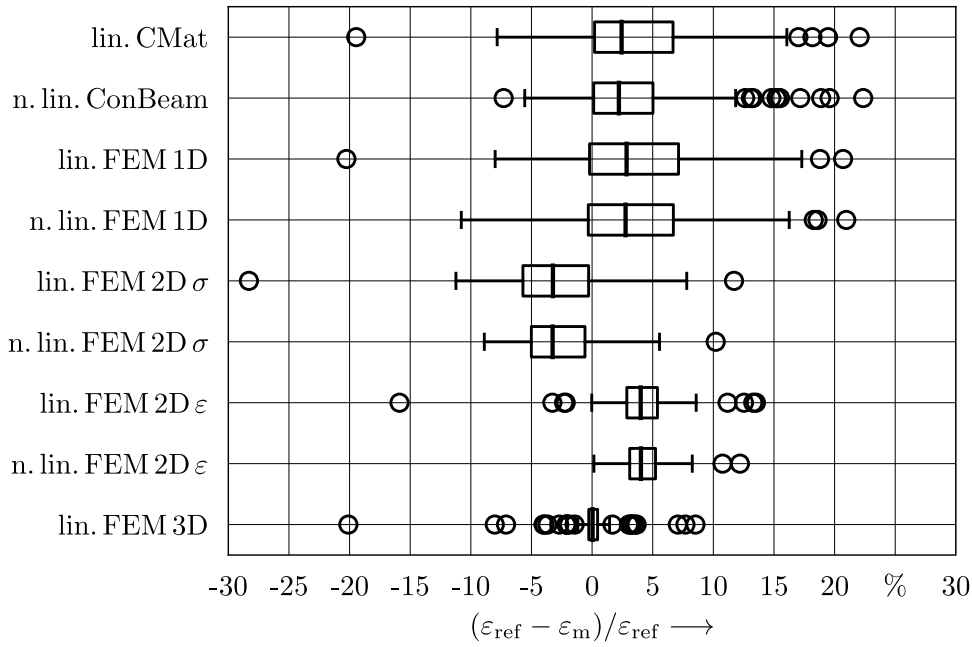


Fig. 8. Signed percentage error of the maximum hinge strain for the evaluated models.

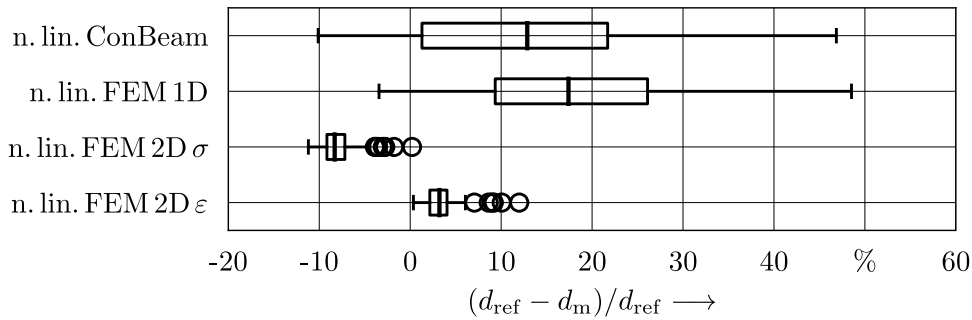


Fig. 9. Signed percentage error of the rotational axis shift for the geometric nonlinear models.

Table 2

Median and the interquartile range of the signed percentage error of the maximum hinge strain ( $MEPE_e$ ,  $IQRPE_e$ ) and rotational axis shift ( $MEPE_d$ ,  $IQRPE_d$ ) as well as the mean computational time ratio ( $t_{ref}/t_m$ ,  $\overline{t_{ref}} = 223.70$  s).

Model	$MEPE_e$ in %	$IQRPE_e$ in %	$MEPE_d$ in %	$IQRPE_d$ in %	$\frac{\overline{t_{ref}}}{t_m}$
lin. CMat	2.43	6.47	11.61	27.06	43592672.33
n. lin. ConBeam	2.21	4.89	12.87	20.42	2070.54
lin. FEM 1D	2.85	7.34	18.23	21.51	15181.14
n. lin. FEM 1D	2.76	7.02	17.40	16.76	4667.86
lin. FEM 2D $\sigma$	-3.23	5.42	-8.73	3.87	54.09
n. lin. FEM 2D $\sigma$	-3.26	4.42	-8.31	1.97	38.26
lin. FEM 2D $\epsilon$	4.01	2.52	2.99	3.75	53.39
n. lin. FEM 2D $\epsilon$	4.03	2.13	3.21	1.89	38.22
lin. FEM 3D	0.04	0.73	-0.17	2.89	4.60

model becomes more similar to the reference model and further physical effects are considered. The comparison of the outliers of the geometrically linear and nonlinear models shows significant differences for individual load cases. These can be attributed to interactions between the loads and deformations, which are not captured by geometrically linear models due to their superposition property. This becomes especially apparent in the case of stability failure due to buckling. Another example are counteracting loads. Positive longitudinal loads lead to a straightening of the hinge and thus counteract large rotation angles. However, for the majority



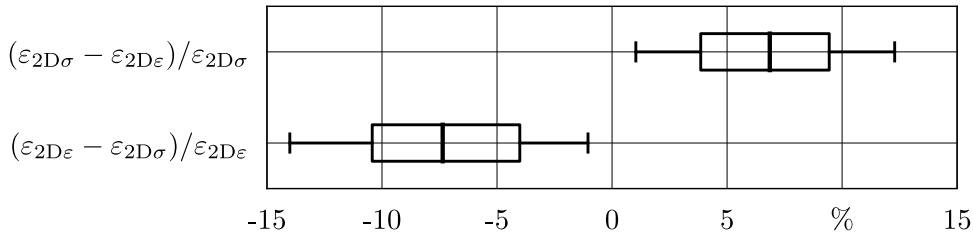


Fig. 10. Relative error of the maximal hinge strain between quadrilateral element models for plane strain (2D  $\epsilon$ ) and plane stress (2D  $\sigma$ ) assumptions.

of load cases and thus for the majority of possible analysis calculations, there are minor differences in the error of the hinge strain between the geometric linear and nonlinear models of the same type.

This, nevertheless, does not apply to the analysis of the rotational axis shift. The nonlinear models are much more accurate in this regard (see Table 2). Although the nonlinear beam models show significant deviations (see Fig. 9), existing studies indicate high accuracy for the analysis of guidance errors of entire mechanisms [7,31]. The multitude of influencing factors on the guidance error (link deformations, deviations of the hinge position in the mechanism, etc.) makes the analysis of the overall mechanism necessary.

However, especially for the early stages of development, the errors of the beam models in the strain calculation might be acceptable. In addition, a significant reduction of the computation time allows a broader exploration of the design solution space by means of optimization. The compliance matrices model according to Lobontiu shows high potential for this purpose, due to the significant reduction of the computation time and the similar accuracy for the analysis of the hinge strain among the beam models. The deviations between the nonlinear beam models (n. lin. ConBeam and n. lin. FEM 1D) result from the chosen number of elements in the finite Euler–Bernoulli beam element model and the slightly different model assumptions. Contrary to the continuum beam models, the derivation of the finite beam models include a small-angle approximation, which can lead to deviations in some load cases. The results further converge and the computation time increases for a higher element number (see Appendix). Most positive outliers of the beam models occur in the case of minor hinge radii and greater hinge heights. This can be explained by the stress concentration in the area of small radii, which become especially apparent in hinges of greater bending stiffness.

Despite the restriction to one hinge length and width, the results can be applied to other hinges. Due to the load case ( $F_x$ ,  $F_y$ ,  $M_z$ ), the quadrilateral element model assumptions of plane strain (FEM 2D  $\epsilon$ ) and plane stress (FEM 2D  $\sigma$ ) can be considered as limit cases for wide ( $w \gg h$ ) and narrow hinges ( $w \ll h$ ). Depending on the hinge width, the results of the hexahedral element model (FEM 3D) lies between the results of these two models, apart from numerical deviations for small strain values (see also [7,9]). The comparison of the quadrilateral element models thus allows the estimation of the range of results of the hexahedral element models for arbitrary hinge widths. This is exemplarily shown in Fig. 10 for the hinge strain error of both quadrilateral models relative to the respective other model. The relative error of the plane strain assumption (suitable for wide hinges where  $w \gg h$ ) relative to the plane stress assumption thus describes the error to be expected when modeling narrow hinges and vice versa. The absolute errors in both cases are approximately distributed around a median of  $\pm 7\%$  and an interquartile range of 6%. A similar comparison for all investigated models or the combination of the results from Fig. 10 and Fig. 8, can be used to estimate the upper relative strain error due to the change in width. Furthermore, the assumption of plane stress results in higher strain values and thus in a negative relative error. This leads to a conservative design for the dimensioning of hinges.

The presented results can also be applied to hinges with a different total length  $l$ . Please note, that the displacements scale linearly with the uniform change in hinge dimensions, under the condition of a constant rotation angle and constant hinge strain [32]. For example, a hinge twice as large would result in the same hinge strains and twice as large rotational axis shift due to the load definition strategy used. The relative error remains unchanged. But nonlinear relationships arise for the evaluation of the torques and hinge forces, which would have to be taken into account for their study. However, the investigations cover a wide range of hinge dimensions and load cases. The results allow an estimation of the error of the maximal hinge strain and rotational axis shift and thus a selection of an analysis model for the given application in the design process. The experimental design, load determination and meshing strategy in this study can also be used in future studies, to extend their general validity.

## Declaration of competing interest

The authors declare that they have no known competing financial interests or personal relationships that could have appeared to influence the work reported in this paper.

## Acknowledgment

The authors would like to thank professor Nicolae Lobontiu for his helpful advice on the modeling of flexure hinges with compliance matrices according to [15].

**Table A.3**Strain error values ( $MEPE_\epsilon$ ,  $IQRPE_\epsilon$ ) and mean computational time ratio ( $\overline{t_{ref}}/\overline{t_m}$ ) for different elements ( $n_e$ ,  $n_k$ ) with constant cross-sectional profile.

$n_e$	$n_k = 2$			$n_k = 3$			$n_k = 4$		
	$MEPE_\epsilon$	$IQRPE_\epsilon$	$\frac{\overline{t_{ref}}}{\overline{t_m}}$	$MEPE_\epsilon$	$IQRPE_\epsilon$	$\frac{\overline{t_{ref}}}{\overline{t_m}}$	$MEPE_\epsilon$	$IQRPE_\epsilon$	$\frac{\overline{t_{ref}}}{\overline{t_m}}$
	in %	in %		in %	in %		in %	in %	
4	-6.38	30.28	36732	-5.76	21.23	26042	-4.88	17.92	17788
6	-5.19	16.40	30116	-4.26	12.10	19750	-3.54	11.90	6805
8	-2.45	13.48	25064	-1.83	10.20	11989	-1.70	9.98	5529
10	-2.24	12.19	20622	-1.31	8.90	6426	-1.19	9.48	4744
12	-1.80	10.55	16292	-1.11	7.94	5740	-1.00	7.89	3768
14	-1.65	9.62	15235	-0.78	7.28	5640	-0.82	7.39	3621
16	-1.57	9.04	13217	-0.96	6.91	4281	-0.96	6.62	2657
18	-1.47	8.06	7008	-0.77	6.42	4060	-0.72	6.24	2696
20	-1.20	8.11	7274	-0.64	6.43	3400	-0.62	6.30	2496

**Table A.4**Strain error values ( $MEPE_\epsilon$ ,  $IQRPE_\epsilon$ ) and mean computational time ratio ( $\overline{t_{ref}}/\overline{t_m}$ ) for different elements ( $n_e$ ,  $n_k$ ) with tapered cross-sectional profile.

$n_e$	$n_k = 2$			$n_k = 3$			$n_k = 4$		
	$MEPE_\epsilon$	$IQRPE_\epsilon$	$\frac{\overline{t_{ref}}}{\overline{t_m}}$	$MEPE_\epsilon$	$IQRPE_\epsilon$	$\frac{\overline{t_{ref}}}{\overline{t_m}}$	$MEPE_\epsilon$	$IQRPE_\epsilon$	$\frac{\overline{t_{ref}}}{\overline{t_m}}$
	in %	in %		in %	in %		in %	in %	
4	-3.77	25.81	36792	-2.06	16.31	26351	-1.39	14.61	14200
6	-0.98	16.34	29796	0.18	12.25	16263	0.10	10.95	6775
8	2.05	11.47	24470	1.75	10.51	10707	1.91	9.88	4316
10	2.32	9.45	19095	3.02	8.53	7380	3.21	8.18	4185
12	2.24	8.86	17242	2.75	7.61	6569	2.72	7.66	2837
14	2.26	8.09	15233	2.76	7.02	4668	2.72	6.97	2628
16	2.32	7.53	13449	2.62	6.52	4491	2.65	6.52	2615
18	2.10	7.37	7658	2.65	6.66	3981	2.79	6.79	2534
20	2.09	6.36	6590	2.75	6.52	3574	2.85	6.89	2093

**Table A.5**Strain error values ( $MEPE_\epsilon$ ,  $IQRPE_\epsilon$ ) and mean computational time ratio ( $\overline{t_{ref}}/\overline{t_m}$ ) for different elements ( $n_e$ ,  $n_k$ ) with circular cross-sectional profile.

$n_e$	$n_k = 2$			$n_k = 3$			$n_k = 4$		
	$MEPE_\epsilon$	$IQRPE_\epsilon$	$\frac{\overline{t_{ref}}}{\overline{t_m}}$	$MEPE_\epsilon$	$IQRPE_\epsilon$	$\frac{\overline{t_{ref}}}{\overline{t_m}}$	$MEPE_\epsilon$	$IQRPE_\epsilon$	$\frac{\overline{t_{ref}}}{\overline{t_m}}$
	in %	in %		in %	in %		in %	in %	
4	-4.01	14.05	19885	-0.57	16.09	5991	2.80	6.75	2402
6	-5.25	12.08	15007	2.11	7.54	4118	2.60	4.72	1639
8	-4.87	10.01	12318	1.98	5.37	3251	2.42	4.72	1297
10	-4.50	9.69	10368	1.89	5.39	2541	2.40	4.72	1092
12	-2.90	8.27	8303	2.11	5.11	2159	2.35	4.77	885
14	-1.92	8.18	7665	2.15	5.10	1950	2.34	4.77	785
16	-1.55	7.32	6751	2.16	4.95	1659	2.41	4.80	703
18	-0.96	7.54	5134	2.19	5.00	1471	2.32	4.87	633
20	-0.55	6.97	4434	2.09	5.00	1350	2.28	4.93	583

## Appendix. Meshing parameters of beam elements

Tables A.3 to A.5 list the median and the interquartile range of the signed percent error of the maximum hinge strain ( $MEPE_\epsilon$ ,  $IQRPE_\epsilon$ ) and rotational axis shift ( $MEPE_d$ ,  $IQRPE_d$ ) as well as the mean computational time ratio ( $\overline{t_{ref}}/\overline{t_m}$ ,  $\overline{t_{ref}} = 223.70$  s) of the nonlinear finite Euler–Bernoulli beam element models (n. lin. FEM 1D) in dependence of element number  $n_e$ , node number  $n_k$  and the contour profile (see Fig. 4).

## References

- [1] L. Zentner, S. Linß, Compliant Systems: mechanics of Elastically Deformable Mechanisms, Actuators and Sensors, De Gruyter Oldenbourg, Berlin, Boston, 2019, <http://dx.doi.org/10.1515/9783110479744>.
- [2] H.-H. Pham, I.-M. Chen, Stiffness modeling of flexure parallel mechanism, Precis. Eng. 29 (4) (2005) 467–478, <http://dx.doi.org/10.1016/j.precisioneng.2004.12.006>.
- [3] Y. Li, Q. Xu, A totally decoupled piezo-driven XYZ flexure parallel micropositioning stage for micro/nanomanipulation, IEEE Trans. Autom. Sci. Eng. 8 (2) (2011) 265–279, <http://dx.doi.org/10.1109/TASE.2010.2077675>.

- [4] Y. Li, Q. Xu, A novel piezoactuated XY stage with parallel, decoupled, and stacked flexure structure for micro-/nanopositioning, *IEEE Trans. Ind. Electron.* 58 (8) (2011) 3601–3615, <http://dx.doi.org/10.1109/TIE.2010.2084972>.
- [5] W. Ai, Q. Xu, New structure design of a flexure-based compliant microgripper, in: 2014 IEEE International Conference on Robotics and Biomimetics, ROBIO 2014, 2014, pp. 2588–2593, <http://dx.doi.org/10.1109/ROBIO.2014.7090731>.
- [6] R.D. Dsouza, K.P. Navin, T. Theodoridis, P. Sharma, Design, fabrication and testing of a 2 DOF compliant flexural microgripper, *Microsyst. Technol.* 24 (9) (2018) 3867–3883, <http://dx.doi.org/10.1007/s00542-018-3861-y>.
- [7] S. Henning, L. Zentner, Analysis of planar compliant mechanisms based on non-linear analytical modeling including shear and lateral contraction, *Mech. Mach. Theory* 164 (2021) 104397, <http://dx.doi.org/10.1016/j.mechmachtheory.2021.104397>.
- [8] R. Friedrich, R. Lammering, T. Heurich, Nonlinear modeling of compliant mechanisms incorporating circular flexure hinges with finite beam elements, *Precis. Eng.* 42 (2015) 73–79, <http://dx.doi.org/10.1016/j.precisioneng.2015.04.001>.
- [9] M.A. Torres Melgarejo, M. Darnieder, S. Linß, L. Zentner, T. Fröhlich, R. Theska, On modeling the bending stiffness of thin semi-circular flexure hinges for precision applications, *Actuators* 7 (4) (2018) 1–16 paper 86, <http://dx.doi.org/10.3390/act7040086>.
- [10] A. Midha, L.L. Howell, T.W. Norton, Limit positions of compliant mechanisms using the pseudo-rigid-body model concept, *Mech. Mach. Theory* 35 (1) (2000) 99–115, [http://dx.doi.org/10.1016/S0094-114X\(98\)00093-7](http://dx.doi.org/10.1016/S0094-114X(98)00093-7).
- [11] X. Pei, J. Yu, G. Zong, S. Bi, An effective pseudo-rigid-body method for beam-based compliant mechanisms, *Precis. Eng.* 34 (3) (2010) 634–639, <http://dx.doi.org/10.1016/j.precisioneng.2009.10.001>.
- [12] S. Awtar, A.H. Slocum, E. Sevincer, Characteristics of beam-based flexure modules, *J. Mech. Des.* 129 (6) (2006) 625–639, <http://dx.doi.org/10.1115/1.2717231>.
- [13] S. Awtar, S. Sen, A generalized constraint model for two-dimensional beam flexures: Nonlinear load-displacement formulation, *J. Mech. Des.* 132 (8) (2010) <http://dx.doi.org/10.1115/1.4002005>.
- [14] N. Lobontiu, *Compliant Mechanisms: Design of Flexure Hinges*, second ed., CRC Press, ISBN: 978-1-4398-9369-2, 2020.
- [15] N. Lobontiu, J.S.N. Paine, E. Garcia, M. Goldfarb, Corner-filleted flexure hinges, *J. Mech. Des.* 123 (3) (2000) 346–352, <http://dx.doi.org/10.1115/1.1372190>.
- [16] S. Henning, S. Linß, P. Gräser, R. Theska, L. Zentner, Non-linear analytical modeling of planar compliant mechanisms, *Mech. Mach. Theory* 155 (2021) 104067, <http://dx.doi.org/10.1016/j.mechmachtheory.2020.104067>.
- [17] Y.K. Yong, T.-F. Lu, D.C. Handley, Review of circular flexure hinge design equations and derivation of empirical formulations, *Precis. Eng.* 32 (2) (2008) 63–70, <http://dx.doi.org/10.1016/j.precisioneng.2007.05.002>.
- [18] S. Linß, P. Schorr, L. Zentner, General design equations for the rotational stiffness, maximal angular deflection and rotational precision of various notch flexure hinges, *Mech. Sci.* 8 (1) (2017) 29–49, <http://dx.doi.org/10.5194/ms-8-29-2017>.
- [19] G. Hao, J. Yu, H. Li, A brief review on nonlinear modeling methods and applications of compliant mechanisms, *Front. Mech. Eng.* 11 (2) (2016) 119–128, <http://dx.doi.org/10.1007/s11465-016-0387-9>.
- [20] M. Ling, L.L. Howell, J. Cao, G. Chen, Kinestatic and dynamic modeling of flexure-based compliant mechanisms: A survey, *Appl. Mech. Rev.* 72 (3) (2020) 1–19 paper 030802, <http://dx.doi.org/10.1115/1.4045679>.
- [21] P. Bilancia, G. Berselli, An overview of procedures and tools for designing nonstandard beam-based compliant mechanisms, *Comput. Aided Des.* 134 (2021) 1–19 paper 103001, <http://dx.doi.org/10.1016/j.cad.2021.103001>.
- [22] W. Hesse, *Aluminium Material Data Sheets*, Beuth Verlag GmbH, ISBN: 978-3-410-26875-8, 2016.
- [23] S. Linß, T. Erbe, R. Theska, L. Zentner, The influence of asymmetric flexure hinges on the axis of rotation, in: *Innovation in Mechanical Engineering – Shaping the Future: Proceedings*, 56. IWK, Ilmenau, ISBN: 978-3-86360-001-3, 2011, URN: urn:nbn:de:gbv:ilm1-2011iwk-006:6.
- [24] R. Friedrich, R. Lammering, M. Rösner, On the modeling of flexure hinge mechanisms with finite beam elements of variable cross section, *Precis. Eng.* 38 (4) (2014) 915–920, <http://dx.doi.org/10.1016/j.precisioneng.2014.06.001>.
- [25] Y. Shen, X. Chen, W. Jiang, X. Luo, Spatial force-based non-prismatic beam element for static and dynamic analyses of circular flexure hinges in compliant mechanisms, *Precis. Eng.* 38 (2) (2014) 311–320, <http://dx.doi.org/10.1016/j.precisioneng.2013.11.001>.
- [26] R. Friedrich, Modellierung und Optimierung nachgiebiger Mechanismen auf Basis elastischer Festkörpergelenke mit Hilfe von nichtlinearen Finiten Balkenelementen, (Ph.D. thesis), Helmut-Schmidt-Universität/Universität der Bundeswehr Hamburg, 2016, <http://dx.doi.org/10.24405/541>.
- [27] S. Xu, X. Zhu, Z. Dong, P. Liu, Nonlinear modeling and analysis of compliant mechanisms with circular flexure hinges based on quadrature beam elements, *Proc. Inst. Mech. Eng. C* 233 (9) (2019) 3277–3285, <http://dx.doi.org/10.1177/0954406218802945>.
- [28] J.N. Reddy, *An Introduction to Nonlinear Finite Element Analysis*, second ed., Oxford University Press, 2014, ISBN: 978-0-19-964175-8.
- [29] M.K. Thompson, J.M. Thompson, Chapter 6 - meshing, in: *ANSYS Mechanical APDL for Finite Element Analysis*, Butterworth-Heinemann, 2017, pp. 181–199, <http://dx.doi.org/10.1016/B978-0-12-812981-4.00006-X>.
- [30] F. Harfensteller, S. Henning, Data - Modeling of corner-filleted flexure hinges under various loads, Vol. V1, Mendeley Data, 2022, <http://dx.doi.org/10.17632/ycmt4w2wpw.1>.
- [31] F. Harfensteller, S. Henning, S. Linß, Vergleich nichtlinearer kontinuums-balkenmodelle mit finiten balkenmodellen für die analyse nachgiebiger mechanisimen, in: I. D-A-CH (Ed.), 7. IFToMM D-A-CH Konferenz 2021: 18./19. February 2021, Online-Konferenz, 2021, <http://dx.doi.org/10.17185/dupublico/74053>.
- [32] S. Linß, P. Gräser, T. Räder, S. Henning, R. Theska, L. Zentner, Influence of geometric scaling on the elasto-kinematic properties of flexure hinges and compliant mechanisms, *Mech. Mach. Theory* 125 (2018) 220–239, <http://dx.doi.org/10.1016/j.mechmachtheory.2018.03.008>.